Advanced Energy Materials

ADVANCED ENERGY MATERIALS
www.advenergymat.de

RESEARCH ARTICLE OPEN ACCESS

Beyond Descriptor-Based AI Design: Sp^2-Hybridized Branched Side Chains Enable Pre-Aggregation–Driven Seeding Effects in Green-Solvent-Processed Organic Solar Cells

Seokhwan Jeong[1] | Donghoo Won[1] | Zhe Sun[1] | Chihyung Lee[2] | Jaewook Kim[3] | Seunglok Lee[1] | Sangjin Yang[1] | Jieun Kim[1] | Keonho Yoon[2] | Dong Young Kim[1] | Yongjoon Cho[4] | Seung-Jae Shin[1] | Hee-Seung Lee[3] | Doo-Hyun Ko[2] | Changduk Yang[1,5,6]

[1]Department of Energy Engineering, School of Energy and Chemical Engineering, Ulsan National Institute of Science and Technology (UNIST), 50 UNIST-gil, Ulju-gun, Ulsan, South Korea | [2]Department of Chemistry, Sungkyunkwan University, Suwon, Gyeonggi, South Korea | [3]Department of Chemistry and InnoCORE AI-CRED Institute, Korea Advanced Institute of Science and Technology (KAIST), 291 Daehak-ro, Yuseong-gu, Daejeon, South Korea | [4]Department of Chemical Engineering, Pohang University of Science and Technology, Nam-gu, Pohang-si, South Korea | [5]Graduate School of Carbon Neutrality, Ulsan National Institute of Science and Technology (UNIST), 50 UNIST-gil, Ulju-gun, Ulsan, South Korea | [6]UNIST InnoCORE AI-Space Solar Initiative, Ulsan National Institute of Science and Technology (UNIST), Ulsan, South Korea

Correspondence: Doo-Hyun Ko (dhko@skku.edu) | Changduk Yang (yang@unist.ac.kr)

Received: 27 January 2026 | **Revised:** 25 March 2026 | **Accepted:** 9 April 2026

Keywords: machine-learning | non-fullerene acceptors | pre-aggregation | seeding effect | sp^2-Hybridized branched side chains

ABSTRACT

Descriptor-based artificial intelligence (AI) has emerged as a paradigm for molecular design in organic solar cells (OSCs); however, it inherently overlooks collective effects governed by bond hybridization, intermolecular coupling, and aggregation thermodynamics. Such effects are encoded at the solution stage, where pre-aggregation of photoactive materials dictates nucleation pathways, phase separation, and molecular ordering during film formation. Herein, we introduce a YBOV non-fullerene acceptor featuring sp^2-hybridized branched side chains that exhibit an unprecedentedly strong solution-state pre-aggregation propensity. This behavior translates into highly ordered solid films with a densely packed crystalline microstructure, enabled by a thermodynamically stabilized core–terminal dimer. As a result, incorporation of YBOV into OSCs not only outperforms the benchmark L8-BO-based device, but also confers an effective nucleation seeding-agent function across diverse host OSC platforms, delivering efficiencies of up to 19.67% via green-solvent processing by alleviating the intrinsic current–voltage trade-off. Machine-learning predictions largely match experimental photovoltaic parameters with a slight upward bias, except for open-circuit voltage , which exhibits anomalous behavior driven by pre-aggregation–driven seeding effects beyond descriptor-based AI. This work establishes sp^2-hybridized branched side chains as a new molecular design principle, introducing pre-aggregation-enabled seeding effects beyond AI prediction and providing a universal strategy for high-performance OSCs.

Seokhwan Jeong, Donghoo Won and Zhe Sun contributed equally to this work.

1 | Introduction

Organic solar cells (OSCs) have emerged as leading candidates for next-generation photovoltaic technologies owing to their solution processability, mechanical flexibility, lightweight nature, and tunable molecular design [1–8]. Among the various strategies explored, the advent and rapid development of A–D–A′–D–A type non-fullerene acceptors (NFAs), typified by the Y6 series, have been particularly transformative, pushing power conversion efficiencies (PCEs) beyond 20% [9–15]. Pre-aggregation of photoactive materials has recently gained attention as a decisive factor in governing nucleation, phase separation, and molecular ordering during film formation [16]. Properly controlled pre-aggregation can act as a template for subsequent crystallization, leading to more ordered molecular packing, finely tuned domain sizes, and enhanced charge-transport networks [17]. However, unlike polymer donors that exhibit chain entanglement and strong intermolecular interactions favoring pre-aggregation in solution, most high-performance NFAs intrinsically lack this behavior. The scarcity of NFAs with strong pre-aggregation thus represents a critical bottleneck that continues to hinder further advances in device performance.

Side-chain engineering is one of the most powerful molecular design strategies to regulate solubility, intermolecular interactions, and aggregation behavior [18–28]. By tuning the length, branching position, or steric volume of alkyl side substituents, it is possible to directly influence π–π stacking distances, molecular orientation, and donor–acceptor phase separation within the photoactive layer. The bulky sp^3-branched alkyl side chains ubiquitously adopted in state-of-the-art NFAs, while effective in ensuring solubility and solution processability, inevitably weaken intermolecular coupling, suppress pre-aggregation in solution, and restrict microstructural control during film formation [29]. This inherent trade-off between solubility and pre-aggregation remains a major obstacle, underscoring the urgent need for innovative side-chain design strategies that simultaneously preserve processability while promoting strong pre-aggregation and directed crystallization. In addition, processing solvent has been increasingly recognized as a critical factor governing the transfer of aggregation behavior into the solid-state thin film microstructure. From this perspective, *o*-xylene was employed as a halogen-free green solvent for processing in this study. Compared with conventional halogenated solvents, *o*-xylene exhibits lower toxicity and higher industrial compatibility, while its relatively high boiling point and limited solubility provide processing conditions that effectively reflect molecular aggregation and stacking behavior in solution.

Motivated by the recognition that sp^2-hybridized branched side chains impart intrinsic rigidity, suppress torsional disorder, and reinforce intermolecular π–π interactions, in this study, we designed and synthesized a novel YBOV NFA that departs from the long-standing reliance on bulky sp^3-branched side chains. Comprehensive spectroscopic and structural analyses revealed that YBOV exhibited exceptionally strong solution-state pre-aggregation, in stark contrast to the benchmark L8-BO with conventional sp^3-branched side chains, which translated into tighter π–π stacking, higher crystal density, and enhanced electron mobility through a thermodynamically stabilized core–terminal dimer. OSC studies confirmed the superior performance of YBOV-based devices compared with L8-BO counterparts. More interestingly, when incorporated into diverse host systems, YBOV functioned as effective pre-aggregation–driven seeds, enlarging domains and enhancing crystallinity, thereby boosting photovoltaic performance and delivering a champion PCE of 19.67% via green-solvent processing. In parallel, machine-learning (ML) framework was developed to predict OSC performance across 750 devices, showing strong agreement with experimental short-circuit current (J_{SC}), fill factor (FF), and PCE values albeit with a modest upward bias; whereas open-circuit voltage (V_{OC}) deviated due to anomalous voltage behavior originating from pre-aggregation–driven seeding effects that are not captured by descriptor-based models. The pre-aggregation–driven seeding effects enabled by sp^2-hybridized branched side chains, as introduced here, provide a unique and broadly applicable pathway to advance OSC performance.

2 | Results and Discussion

2.1 | Synthesis and Characterization

Figure 1a depicts L8-BO and YBOV, which are isostructural at the conjugated backbone and outer side chains but differ at the inner side chains. The benchmark high-performance L8-BO NFA features conventional sp^3-branched side chains at both the inner and outer positions, whereas YBOV incorporates sp^2-hybridized branched inner side chains. Starting from ethyl-3-ethylhept-2-enoate, the key sp^2-hybridized branched side chain precursor, 1-bromo-3-ethylhept-2-ene (3), was synthesized via a three-step route. The target YBOV was subsequently prepared following the established Y6-series protocol, employing sequential transformations including Stille cross-coupling, Cadogan reductive cyclization, alkylation, Vilsmeier–Haack formylation, and final Knoevenagel condensation. Synthetic details and full characterization data are available in Figure 1b and Supporting Information (NMR, MALDI-TOF MS). Relative to L8-BO (−5.75/−3.89 eV), the YBOV showed slightly upshifted HOMO/LUMO energy levels (−5.66/−3.80; from cyclic voltammetry; Figure S1), indicative of the regulated solid-state packing imparted by the sp^2-hybridized branched side chains.

To the impact of sp^2-hybridized branched side chains on intermolecular interactions, we comparatively examin the optical properties of L8-BO and YBOV (Figure 1c). To access molecular absorption in the monomeric state with negligible intermolecular interactions, UV–vis spectra were first recorded in dilute solutions (0.02 mM) [30]. Both NFAs exhibited nearly identical (0–0) absorption maxima at 732 nm, similar onsets, and strong absorption across 550–800 nm. Upon increasing concentration from 0.02 to 0.64 mM, YBOV exhibited a pronounced growth of the shoulder peak at 680 nm, with the I_{680}/I_{732} ratio rising from 0.45 to 0.57, evidencing enhanced intermolecular interactions and a propensity for pre-aggregation in solution [31–33]. By contrast, L8-BO showed negligible spectral or intensity changes over the same concentration range, consistent with monomeric behavior in solution. In the solution state, the solvent molecular movement can obscure intermolecular interactions and their associated electronic transitions. To overcome this limitation, UV–vis absorption spectra were measured in a polymer matrix, which suppresses

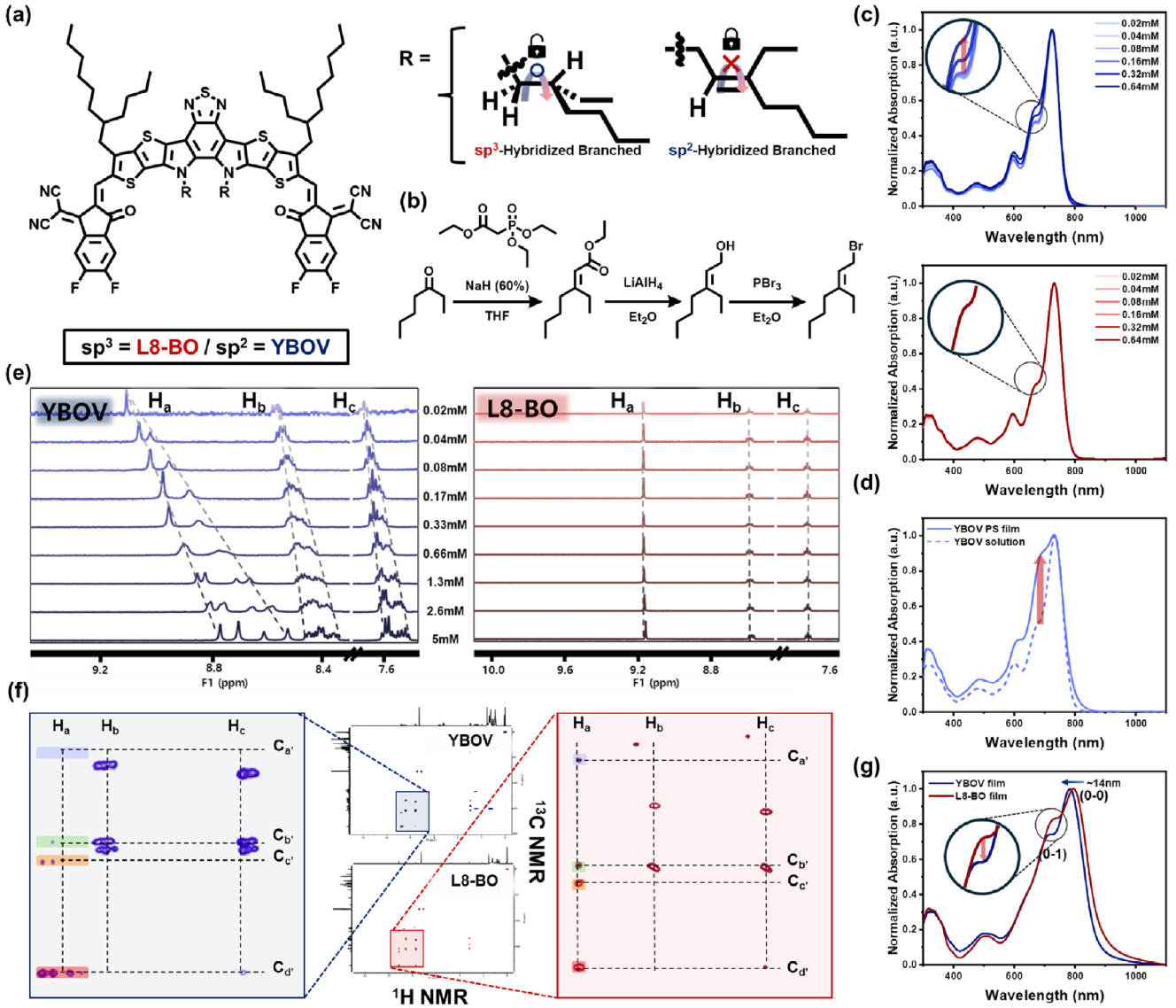

FIGURE 1 | (a) Chemical structures of L8-BO and YBOV. (b) Synthetic route of sp^2-hybridized branched side chain. (c) Normalized absorption spectra of YBOV and L8-BO in *o*-xylene solution. (d) UV–vis absorption spectra for YBOV polystyrene film (0.32 mM). (e) Concentration-dependent ^1H NMR spectra of YBOV and L8-BO (c = 0.02–5 mM) in $CDCl_3$. (f) ^{13}C–^1H correlation spectra NMR spectra of YBOV and L8-BO by HMBC measurement. (g) Normalized absorption spectra of YBOV and L8-BO in thin film.

molecular mobility and minimizes solvent effects, thereby providing a more static environment for analyzing pre-aggregation structures (Figure 1d) [31]. In this experiment, polystyrene was selected as the polymer matrix because it contains a phenyl moiety resembling that of *o*-xylene, a solvent used in device fabrication, while showing no spectral interference within the absorption region of the acceptor. Furthermore, the composition concentrations were designed by considering both the average intermolecular distance and phenyl moiety density, allowing comparison of interaction differences across concentrations. UV–vis absorption spectra measured in the polymer matrix revealed that YBOV exhibited more pronounced pre-aggregation behavior than observed in solution. Specifically, within the matrix, the shoulder peak at 680 nm increased markedly, with the I_{680}/I_{732} ratio rising from 0.506 to 0.901, accompanied by a slight red shift in the absorption onset. These results indicate that confinement within the polymer matrix restricts molecular mobility, thereby promoting pre-aggregation of YBOV, enhancing the shoulder peak intensity, and altering the optical properties.

To further clarify the molecular pre-aggregation in the solution state, ^1H NMR spectra were recorded over a concentration range from 0.02 to 5 mM (Figure 1e and Figure S2). With increasing concentration, YBOV exhibited pronounced upfield chemical shifts, most notably for H_a (9.107 → 8.77–8.53 ppm) associated with the vinylene π-bridge in the conjugated backbone, as well as for H_b and H_c of the 3-(dicyanomethylene) indanone terminal groups, whereas L8-BO remained nearly unchanged. Besides, YBOV exhibited increased complexity in proton signal multiplicity at higher concentrations, exemplified by H_a transitioning from a singlet to a doublet of doublets. These features collectively indicate a strong propensity of YBOV toward pre-aggregation, governed by π–π stacking interactions involving the

surrounding terminal groups [34, 35]. To gain deeper insight into the solution-state molecular pre-aggregation behavior, we also recorded heteronuclear multiple bond correlation (HMBC) spectra for the two NFAs at high concentration (5 mM) (Figure 1f and Figure S3), with the J-coupling constant set to ~10 Hz to resolve ^{13}C–^{1}H couplings separated by two or more bonds. In the HMBC spectra, L8-BO showed clear heteronuclear correlations between carbons ($C_{a'}$, $C_{b'}$, $C_{c'}$, and $C_{d'}$) in the vicinity of the terminal groups and the corresponding H_a, H_b, and H_c. It should be noted, however, that the apparent H_b and H_c correlation in the $C_{b'}$ region cannot be assigned unambiguously due to signal overlap from neighboring carbons ($C_{e'}$ and $C_{f'}$) (Figure S4). In contrast, in YBOV, the HMBC signals for carbons adjacent to H_a were either absent or markedly attenuated, attributable to local electronic changes such as reduced J-coupling efficiency and accelerated relaxation processes induced by pre-aggregation [36].

In the solid film, absorption extended to ~900 nm, and YBOV displayed a 14 nm blue shift in both absorption maximum and onset relative to L8-BO (Figure 1g). Moreover, the relative intensity ratio of the (0–0) to (0–1) vibronic transitions revealed stronger intermolecular electronic coupling for YBOV. A higher (0–0)/(0–1) ratio is generally associated with enhanced π–π interactions and closer molecular packing, since intermolecular electronic coupling stabilizes the lowest-energy transition while suppressing higher vibronic transitions [37, 38]. This trend indicates that YBOV undergoes more effective aggregation and tighter molecular packing during film formation compared with L8-BO.

2.2 | Crystal Structures and Film Properties

Single-crystal X-ray diffraction (SCXRD) analysis was carried out to investigate how variations in side-chain hybridization (sp^3 vs. sp^2) affect the molecular crystal structures and packing motifs. A high-quality single crystal of YBOV was grown by slow diffusion of acetone into a dibromomethane solution, whereas the crystal structure of L8-BO was retrieved from the Cambridge Crystallographic Data Centre (CCDC No. 2005533). As illustrated in Figure 2a, the alignment of five molecular units along the horizontal and diagonal directions yielded a YBOV lattice (33.876 Å × 68.000 Å) distinguished by pronounced compactness along the horizontal axis, whereas L8-BO crystallized into a broader lattice (54.871 Å × 50.440 Å) exhibiting nearly isotropic packing across both orientations [39]. To shed light on the divergent packing structures (Figure 2b), we examined the π–π stacking dimeric configurations. YBOV was found to adopt two distinct dimeric configurations: a core–terminal dimer, in which both the core and terminal segments of one molecule simultaneously overlap with the conjugated core and terminal regions of another, and a terminal–terminal dimer oriented diagonally. By contrast, the L8-BO crystal exhibited three dimeric configurations, comprising a core–core dimer and two types of terminal–terminal dimers oriented diagonally and horizontally, respectively.

Binding energy calculations from molecular dynamics simulations revealed that YBOV strongly favors the more stable core–terminal dimer (−3.012 eV) over the terminal–terminal dimer (−1.245 eV), whereas L8-BO forms the core–core dimer (−2.302 eV) along with terminal–terminal counterparts (−1.524 and −1.605 eV). As a result, YBOV establishes effective and continuous pathways in the vicinity of the terminal regions, supported by higher LUMO electron densities arising from multifaceted intermolecular interactions (core–core, core–terminal, and terminal–terminal) [40]. In contrast, L8-BO predominantly relies on terminal–terminal interactions, which interrupt pathway continuity and force charges to detour through intramolecular routes before re-entering terminal-based channels. These mechanisms are schematically illustrated in Figure 2c. Consequently, YBOV exhibited a higher crystal density (1.282 mg/mm^3) than L8-BO (1.248 mg/mm^3), translating into enhanced electron mobility (μ_e) determined by space-charge-limited-current (SCLC) method (4.76×10^{-5} cm^2 V^{-1} s^{-1} vs. 3.92×10^{-5} cm^2 V^{-1} s^{-1} for YBOV- and L8-BO-only films, respectively; Figure S5) [11].

To correlate the crystal packing with film crystallinity and orientation, grazing-incidence wide-angle X-ray scattering (GIWAXS) was conducted on neat NFA films (Figure 2d,e). Both NFA films exhibited a predominant face-on orientation, as reflected by a pronounced (010) π–π stacking peak in the out-of-plane (OOP) direction, with d-spacings of 3.55 Å (YBOV) and 3.58 Å (L8-BO) and corresponding crystallite coherence lengths (CCLs) of 27.0 and 19.9 Å, respectively, together with distinct (110)/(11−1) lamellar peaks in-plane (IP). Upon closer inspection, we also found that in addition to the azimuthally oriented (021) peaks observed for both films, YBOV exclusively exhibited an additional OOP peak at $q = 0.861$ Å^{-1}, along with IP peaks at $q = 0.589$ and 1.003 Å^{-1}, signifying more robust π–π interactions and superior crystalline properties.

2.3 | Organic Solar Cells

To evaluate the influence of the side-chain hybridization (sp^3 vs. sp^2) on photovoltaic performance, OSC devices based on bulk-heterojunction (BHJ) active layer were fabricated in a conventional structure of glass/ITO/PEDOT:PSS/active layer/H75/Ag. The active layer comprised a blend of the D18 donor polymer and NFAs dissolved in *o*-xylene with CS_2 (Figure S6 for the polymer donor D18 and N3). 1,4-diiodobenzene (DIB), corresponding to 60% of the total blend solution weight, was incorporated, followed by thermal annealing at 100°C for 2 min. Detailed optimization procedures are described in the Supporting Information. The current–voltage (*J*–*V*) characteristics of the optimized devices under AM 1.5G illumination (100 mW cm^{-2}) are shown in Figure 3a, and the corresponding photovoltaic parameters are summarized in Table 1. The L8-BO-based device showed a PCE 17.04%, with J_{SC} of 24.45 mA cm^{-2}, a V_{OC} of 0.868 V, and a FF of 80.26%. The YBOV-based device delivered an improved PCE of 17.64%, accompanied by a markedly increased V_{OC} of 0.926 V, which is ascribed to the synergistic effect of the unique intermolecular packing and the upshifted LUMO energy levels of YBOV. However, the PCEs were constrained by insufficient current density, which motivated us to further study ternary blends based on the well-established high-current density D18:N3 system. Under the same processing conditions (*o*-xylene/CS_2/DIB), the N3-based binary system achieved a PCE of 17.53%, with a very high J_{SC} of 27.18 mA cm^{-2} as reported and expected, yet a somewhat low V_{OC} and comparable FF values relative to YBOV- and L8-BO-based devices. Through precisely controlled composition tests (Figures S7,S8, Tables S1, S2, and S3), both the L8-BO and

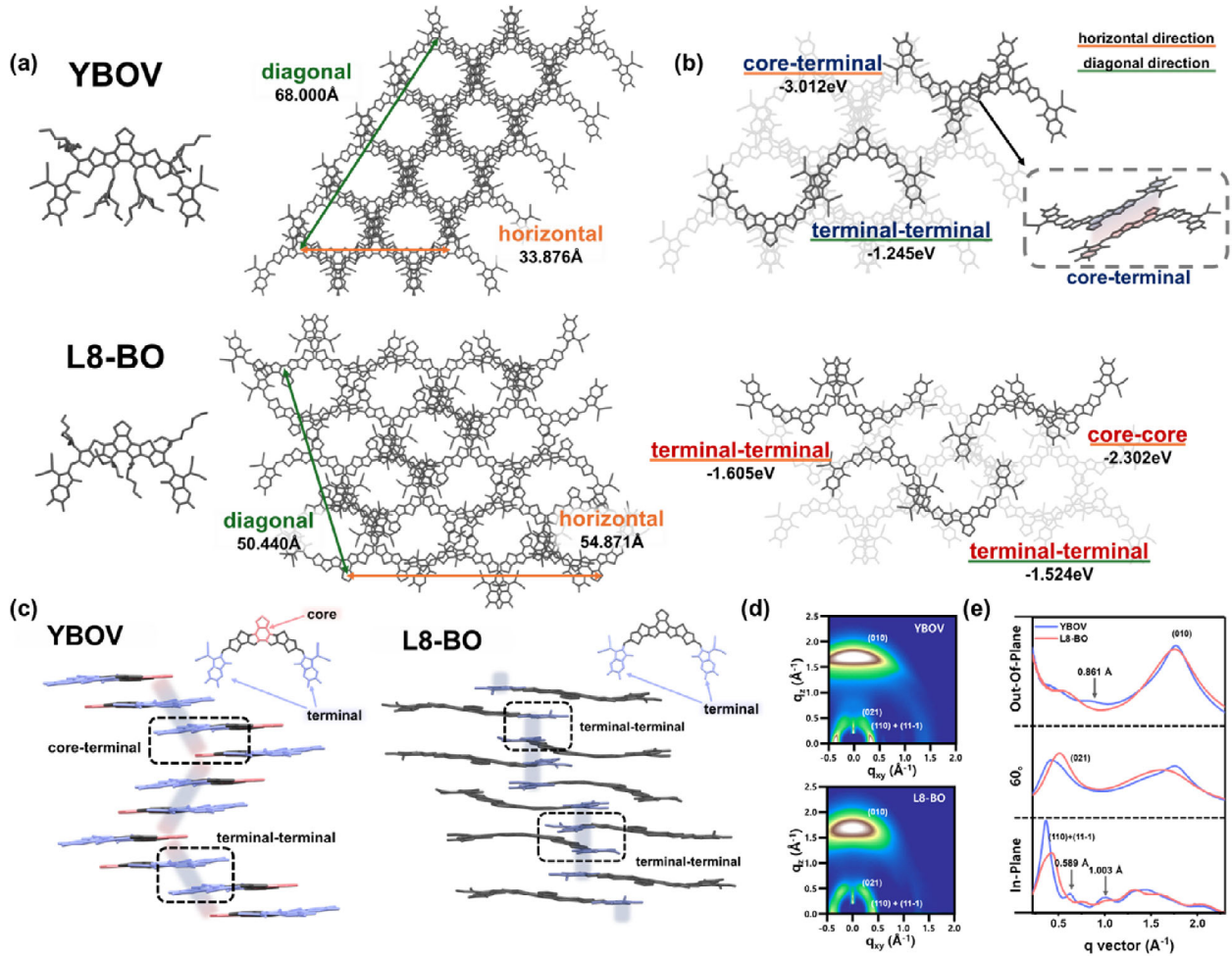

FIGURE 2 | (a) Main view of single-crystal packing of YBOV and L8-BO. (b) Dimeric configurations in the single-crystal structures of YBOV and L8-BO. (c) Side view of single-crystal packing of YBOV and L8-BO. (d) 2D GIWAXS patterns of YBOV and L8-BO. (e) GIWAXS line-cut profiles of YBOV and L8-BO.

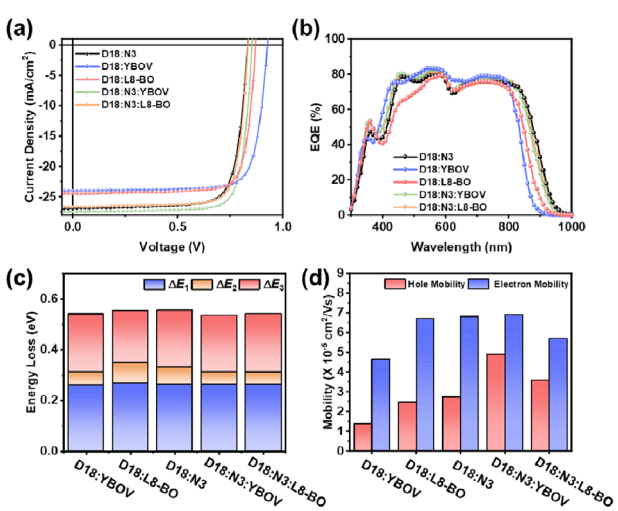

FIGURE 3 | (a) *J*–*V* characteristics and (b) EQE spectra of the optimized OSCs. (c) The total energy loss of D18:N3, D18:YBOV, D18:L8-BO, D18:N3:YBOV, and D18:N3:L8-BO devices. (d) Hole and electron mobilities of the OSCs.

YBOV ternary systems were optimized at a content of 30 wt.%. However, while the L8-BO-based ternary system showed little improvement over its binary counterpart due to a fundamental J_{SC}–*V*oc trade-off that limited the maximum attainable PCE, the optimized YBOV-based ternary device achieved a champion PCE of 18.74%, enabled by the concurrent realization of enhanced J_{SC} and adequately preserved *V*oc (PCE of 19.02% with 2PACz). As shown in Figure 3b and Table 1, the calculated J_{SC} values from external quantum efficiency (EQE) spectra are in good agreement with those measured from the *J*–*V* curves.

To elucidate the origin of the performance differences, we conducted a series of comprehensive studies. First, in addition to extracting the optical bandgaps (E_g) from the EQE spectra, we measured the electroluminescence external quantum efficiency (EQE_{EL}) of the optimized blended films (Figure S9) to quantify total energy loss (E_{loss}). The E_{loss} is evaluated according to the equation $E_{loss} = \Delta E_1 + \Delta E_2 + \Delta E_3$, where ΔE_1 originates from the inevitable radiative recombination defined by the Shockley–Queisser limit, ΔE_2 corresponds to additional radiative recombination below the bandgap, and ΔE_3 accounts for nonradiative recombination. In the case of ΔE_3, the value is determined using the relation ($\Delta E_3 = -kTln(EQE_{EL})$) [41].

TABLE 1 | Photovoltaic parameters of optimized OSCs under illumination of AM 1.5G, 100 mW cm^{-2}.

Active Layer	V_{OC}[a] [V]	J_{SC}[a] [mA cm-2]	J_{cal} [mA cm-2]	Fill Factor[a] [%]	PCE[a] [%]
D18:N3	0.821 (0.825)	27.18 (26.13)	25.83	78.46 (78.64)	17.53 (16.96)
D18:YBOV	0.926 (0.926)	23.99 (23.59)	22.81	79.32 (79.08)	17.61 (17.28)
D18:L8-BO	0.868 (0.867)	24.45 (23.96)	23.38	80.26 (79.45)	17.04 (16.50)
D18:N3:YBOV (30%)	0.853 (0.851)	27.47 (27.40)	25.91	79.99 (79.58)	18.74 (18.56)
D18:N3:L8-BO (30%)	0.831 (0.831)	26.65 (26.42)	25.36	79.78 (79.74)	17.68 (17.50)

[a]The average device values are obtained from 12 cells.

As summarized in Figure 3c and Table S4, while the N3-based binary device had a lower E_{loss}, primarily due to its notably reduced ΔE_2 compared with the other binary counterparts, the YBOV-based binary device showed the lowest ΔE_3 of 0.206 eV, its optimized ternary device achieved the lowest E_{loss} of 0.535 eV with simultaneously low ΔE_2 and ΔE_3. These findings substantiate that the N3-based binary device primarily alleviates radiative recombination, whereas the L8-BO- and YBOV-based counterparts serve to suppress nonradiative recombination losses. Remarkably, the optimized YBOV-based ternary system achieves a concurrent reduction of both radiative and nonradiative recombination pathways [42].

The charge recombination mechanism is further investigated by correlating the illumination intensity (P_{light}) and V_{OC} of the devices (Figure S10). According to equation $V_{OC} \propto n(kT/q)\ln(P_{light})$ (where k, T, and q denote the Boltzmann constant, the absolute temperature, and the elementary charge, respectively), the fitted ideality factor (n) values of the binary systems follow the order N3< L8-BO < YBOV, being consistent to their increasing E_g. Interestingly, the YBOV-based ternary system exhibited a n value approaching unity, indicative of suppressed monomolecular (trap-assisted) recombination. This finding indicates that YBOV incorporation into the N3 binary platform fosters a more favorable domain morphology within the active layer, despite the concomitant E_g enlargement.

As observed for their n values above, both the hole mobility (μ_h) and μ_e in the optimized blended films increased in the order: YBOV ternary > L8-BO ternary > N3 binary > L8-BO binary > YBOV binary (Figure 3d and Table S5). When comparing the binary systems, the N3-based device proves particularly effective in facilitating charge transport across donor–acceptor interfaces, thereby yielding the enhanced J_{SC}. Note that upon incorporating YBOV into the N3 binary platform, the μ_h was markedly increased while the μ_e was retained, leading to the highest μ_h/μ_e as 0.71, which underpins its superior device performance. The origins of these advantageous charge transport and dynamic properties can be further rationalized by the morphological studies described below.

2.4 | Machine-Learning Prediction

To further examine the effect of side-chain hybridization (sp^3 vs. sp^2) on device performance, we employed an ML framework trained on molecular structure descriptors. Figure 4a presents the overall workflow of the OSC-ML models used to predict photovoltaic parameters directly from molecular structure information [43, 44]. The process begins with the assembly of a curated OSC dataset, in which device-level photovoltaic parameters (V_{OC}, J_{SC}, and FF) were extracted from peer-reviewed reports under 1 sun AM 1.5G illumination. The dataset incorporates both molecular structures and composition information. Entries were selected from BHJ-based devices fabricated under solution processing (spin-coating) conditions to ensure reliable structure–property correlations. Among the various BHJ OSC systems, we chose binary and ternary (one donor: two acceptors) blends (325 and 425 combinations; a total of 750 candidate OSCs). For molecular encoding, we used extended connectivity fingerprints (ECFPs) as descriptors. ECFPs represent molecular structures as connectivity-based bit vectors that capture the presence of local atomic or functional-group environments and their neighborhood relationships [45]. These fingerprint vectors were then used as input features for model training. Compared with other molecular descriptors, ECFPs provide a more generalizable and chemically intuitive representation, particularly well-suited for detecting the influence of subtle structural variations. In the present study, this choice was motivated by our focus on verifying whether targeted functional-group substitutions (particularly inner side-chain modification) translate into measurable changes in device performance. To construct the full input set for model training, the generated ECFP-based bit vectors (i.e., molecular descriptor) of each component were weight-averaged. Model construction was then carried out using the *XGBoost* algorithm with 10 fold cross-validation. *XGBoost* is a gradient-boosted decision tree method that sequentially builds an ensemble of weak learners to minimize prediction error while incorporating regularization to prevent overfitting. This approach was selected because it effectively captures non-linear relationships while reducing overfitting, thereby ensuring robust predictive performance. Within this framework, separate sub-models were trained for V_{OC}, J_{SC}, and FF, respectively, and the predictive performance of the OSC-ML models was evaluated.

Figure 4b,c show strong agreement between predicted and experimental values for V_{OC} and J_{SC}. The coefficients of determination (R^2) were 0.77 for V_{OC} and 0.85 for J_{SC}, with values closer to 1 meaning that the models more reliably captured the experimental trends. Although the ML model yielded comparatively lower R^2 values for FF (Figure 4d), the accuracies determined within parameter-specific tolerance thresholds (±0.05 V for V_{OC}, ±2 mA cm^{-2} for J_{SC}, and ±5% for FF) remained consistently high, reaching 87.73% for V_{OC}, 82.80% for J_{SC}, with a moderate 77.60% for FF, thus attesting to the overall robustness and reliability of the framework [46]. In addition, we calculated the PCEs

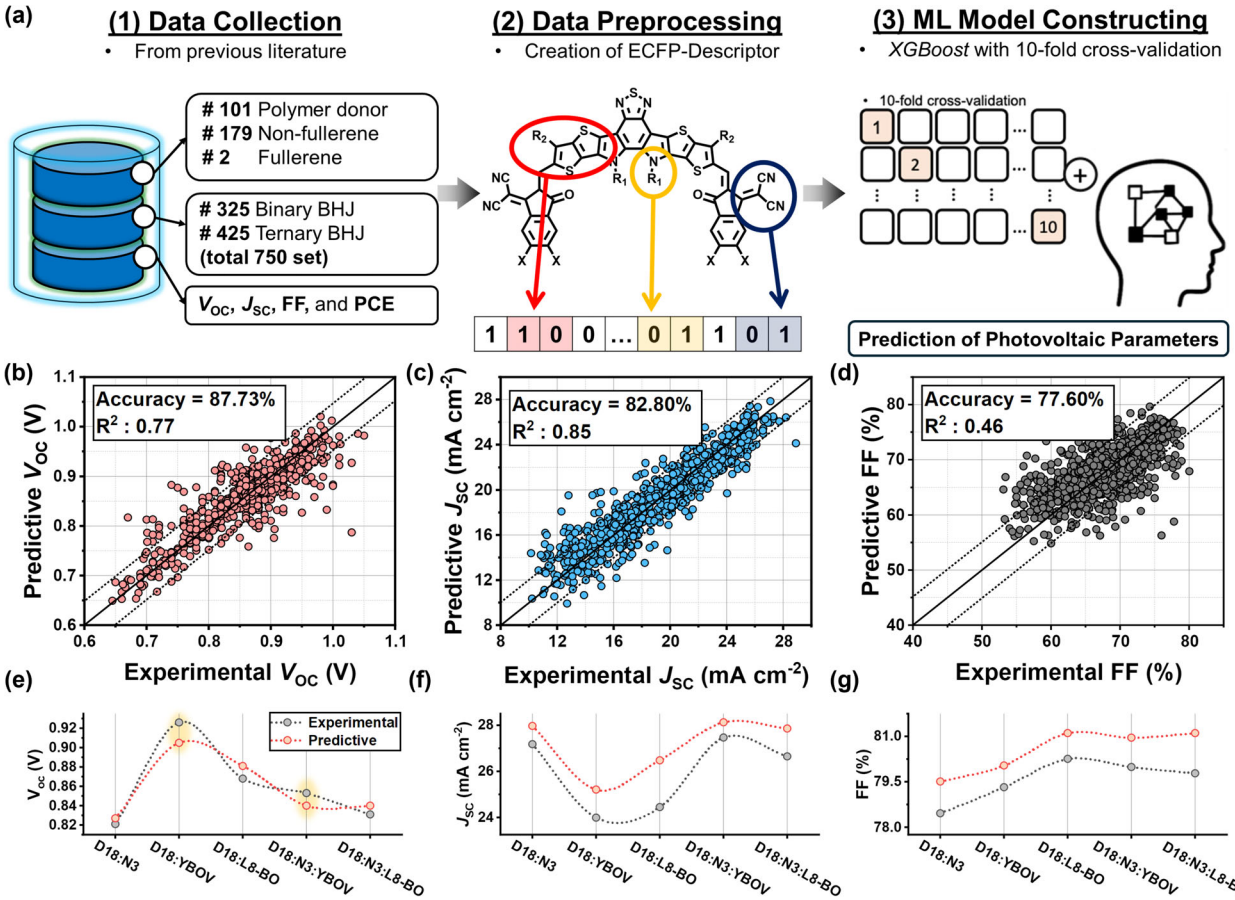

FIGURE 4 | (a) Schematic workflow of the OSC-ML framework: data collection from literature, molecular encoding using ECFPs, and model constructing using *XGBoost* with 10-fold cross-validation. Correlations between experimental and predicted values for (b) V_{OC}, (c) J_{SC}, and (d) FF, respectively. The diagonal solid line indicates a perfect positive correlation, in which the predicted values are equivalent to the experimental values (R^2 = 1.0). The band within diagonal upper and lower dash lines denotes absolute tolerances (= predicted value − experimental value) (±0.05 V for V_{OC}, ±2 mA cm^{-2} for J_{SC}, and ±5% for FF). Comparison of experimental and predicted values for (e) V_{OC}, (f) J_{SC}, and (g) FF in representative binary and ternary OSCs.

by multiplying the individually predicted V_{OC}, J_{SC}, and FF and dividing by the input power (100 mW cm^{-2}), achieving an accuracy of 80.27% within ±1.5% tolerance (Figure S12a), identical to those produced by a dedicated ML model trained directly on PCEs (Figure S12b). This strong consistency confirms that the multiplicative approach provides physically consistent and reliable predictions, reinforcing the robustness and internal coherence of the framework.

Using this validated ML framework, we investigated the structure–performance relationships by comparing predicted outputs with experimental photovoltaic parameters of both binary and ternary blends, measured under the conditions shown in Figure 3a and illustrated in Figure 4e–g for direct comparison of their values. Across all the compositions, the predicted photovoltaic parameters closely mirrored the experimental data, albeit higher than the experimental values. Notably, however, YBOV-containing systems such as D18:YBOV and D18:N3:YBOV showed the opposite trend in V_{OC}, yielding lower predicted V_{OC} values relative to the experiments. Because the ML model employed in this study was trained on ECFPs, the systems with highly similar molecular backbones (e.g., N3, L8-BO, and YBOV) were expected to produce similar prediction trends under typical solution-processing conditions represented in the training dataset. The dataset largely consisted of devices fabricated using volatile solvents such as chloroform and chlorobenzene, where active layer morphology is generally governed by intrinsic molecular structure. Consequently, the model effectively provided a structure-based baseline expectation for photovoltaic behavior. Nevertheless, the experimental results for the YBOV-containing systems deviated from this baseline, suggesting the presence of additional physical effects that are not encoded in the structural descriptors alone [47]. We posit that this divergence in V_{OC} stems from the favorable influence of strong pre-aggregation behavior induced by the sp^2-hybridized branched side chains of YBOV during actual OSC fabrication, an effect that lies beyond the predictive capability of current ML models.

2.5 | Film Formation Kinetics

In situ photoluminescence (PL) measurements were performed to investigate the effect of side-chain hybridization on the kinetics of the blended film formation. The excitation wavelength was set to 660 nm to electively probe the photophysical behavior of the

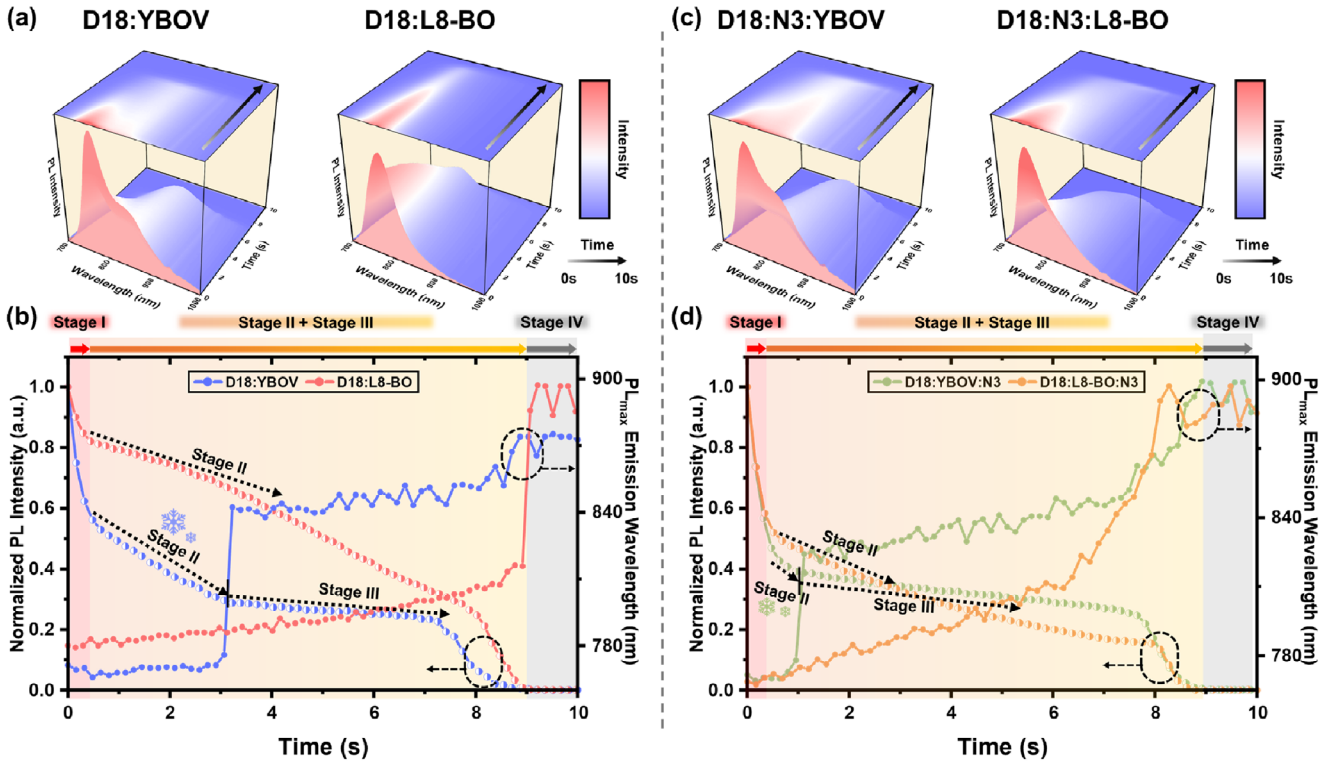

FIGURE 5 | (a) Time evolution 2D contour plots of D18:YBOV and D18:L8-BO. (b) Extracted parameters of D18:YBOV and D18:L8-BO. (c) Time evolution 2D contour plots of D18:N3:YBOV and D18:N3:L8-BO. (d) Extracted parameters of D18:N3:YBOV and D18:N3:L8-BO.

NFAs during film formation under the device-fabrication processing solvents (*o*-xylene/CS_2). Note that all the NFAs showed nearly identical surface energies (41.08–41.61 mJ/m^2), as determined from contact angle measurements, leading to similar miscibility with D18 (Figure S13 and Table S6). As shown in Figure 5a,b, Figures S14 and S15, analysis of the normalized PL intensity and PL maximum emission (PL_{max}) wavelength allowed the film-formation process to be divided into four stages: initial (stage I), stage II, stage III, and final film (stage IV) [48–50]. During stage I (0–0.55 s), the PL intensity decreased sharply due to the rapid evaporation of CS_2 solvent, which has a high vapor pressure (48.1 kPa at room temperature (RT)). This produced a pronounced negative slope, reflecting the rapid approach and interaction of D18 and NFA molecules. In stage II (0.55–3.13 s) and stage III (3.13–8.92 s), the negative slope of PL quenching became less steep as *o*-xylene (vapor pressure: 0.67 kPa at RT) evaporated after CS_2. This progressive evaporation reduced the intermolecular distance between D18 and NFA molecules, thereby promoting PL quenching and facilitating enhanced molecular ordering.

In the YBOV-based binary film, the PL intensity exhibited two distinct regimes during stage II and stage III: in stage II, it declined with an almost constant slope, whereas in stage III, the slope gradually steepened over time. By contrast, the L8-BO- and N3-based binary films displayed a continuous decrease in PL intensity with an already progressively steepening slope from stage II onward, closely resembling the behavior observed in stage III of the YBOV-based film.

Assuming negligible pre-aggregation in the solution state and constant donor–acceptor interactions, the solvent evaporation process can be described as diffusion-governed according to Fick's second law [51]. In this regime, the cumulative evaporated volume is proportional to $\sqrt{t}$, such that the remaining solvent volume can be expressed as $V_0 - k\sqrt{t}$. Substituting this relation into the Stern–Volmer equation gives:

$$I = \frac{I_0}{1 + \frac{K_q \Gamma_0 n}{V_0 - k\sqrt{t}}} \quad (1)$$

where I represents the PL intensity at time t, I_0 the initial intensity, K_q the quenching constant, Γ_0 the initial molecular density, n, the effective number of molecules contributing at a specific wavelength, V_0 the initial solvent volume, and k, the evaporation rate constant, respectively [52].

In the presence of pre-aggregation, the effective number of contributing n decreases, which accelerates the decay of I. In the absence of pre-aggregation, the PL intensity decreases gradually at first and then, with an increasingly steep slope over time, progresses (Figure S16). Stage III of YBOV-based binary and stage II of L8-BO- and N3-based binary counterparts followed the ideal case with constant n, whereas stage II of YBOV-based binary deviated from this behavior, indicating the presence of pre-aggregation where n evolves over time.

The PL_{max} wavelength was also monitored to track the film-formation process. The YBOV-based binary exhibited two distinct PL_{max} features at 770 nm and 842–872 nm, whereas the L8-BO-based binary showed a single PL_{max} at 780–815 nm. In contrast, the N3-based binary displayed two distinct PL_{max} features at 777 nm

and 833–888 nm, which correlated well with the time regimes defined by the PL intensity evolution (stage II and stage III).

For the YBOV-based binary, the onset of the growth stage was delayed due to pre-aggregation, which reduced the number of molecules contributing to the monomeric-state peak and thereby prolonged stage II. During this stage, the PL_{max} remained unchanged at 770 nm without a red shift. A red shift emerged only in stage III, signifying crystal growth and the development of the film microstructure. In contrast, the L8-BO-based binary demonstrated a simpler crystallization pathway in which the decreasing intermolecular distance between donor and acceptor molecules directly promoted aggregation and crystal growth during the transition from stage III to stage IV. Consequently, a red shift of the PL_{max} from 780 to 815 nm was already observed starting from stage I, and in stage IV, film formation was accompanied by the completion of the overall microstructure. For the N3-based binary, crystal growth was initiated as early as stage II, facilitated by the inherently high crystallinity of N3. During stage I, the rapid evaporation of highly volatile CS_2 significantly reduced the intermolecular distance among N3 molecules, thereby triggering aggregation. As a result, in stage II, the PL_{max} exhibited a pronounced red shift to 833–888 nm, signaling the onset of crystal growth and the formation of the film microstructure.

On the other hand, in the ternary systems (*i.e.*, YBOV or L8-BO incorporation into N3 binary platform), YBOV-based ternary showed a stage I (0–0.52 s), followed by a sequentially shortened stage II (0.52–1.03 s; PL intensity decreased with an almost constant slope, with $PL_{max} \approx 770$ nm), stage III (1.03–8.82 s; PL intensity initially moderated but progressively steepened, accompanied by a red-shifted PL_{max} at 823–890 nm), and the stage IV (b and Figure S17). By contrast, the L8-BO-based ternary displayed only two stages (stage II and stage IV), characterized by a continuous decrease in PL intensity from stage II onward and a red shift of PL_{max} from 770 to 887 nm, closely resembling the stage III behavior observed in the YBOV-based binary [53].

These results indicate that when YBOV is incorporated into the N3 binary blend, a distinct stage II emerges due to pre-aggregation, thereby providing additional time for acceptor–acceptor aggregation. In contrast, with L8-BO incorporation, the distinction between stages II and III vanishes, and film formation proceeds through alloy-like behavior driven by the continuous reduction of intermolecular distances.

Although the films at final stage IV exhibited comparable PL_{max} values, their pathways and mechanisms of microstructural development differed markedly. In the case of YBOV, the seed-based stepwise growth mechanism enables more controlled domain formation, whereas L8-BO relies on a continuous distance-reduction pathway, which may be relatively limited in terms of microstructural control. Thus, the pre-aggregation induced by sp^2-hybridized branched side chains acts as seeds during film formation, modulating the trajectory of microstructural development and offering an effective strategy for achieving more precise control over domain formation.

2.6 | Blend Morphology and Microstructure

Tapping-mode atomic force microscopy (AFM), transmission electron microscopy (TEM), and GIWAXS measurements were performed to analyze the surface and bulk morphology and crystallinity of the blended films, as shown in Figure 6. AFM images of all blends revealed a fibrillar surface morphology, while TEM clearly visualized nanoscale phase separation with well-developed bicontinuous networks (Figure 6a) [54]. The binary films exhibited comparable domain sizes of 80–110 nm. Upon ternary incorporation, YBOV enlarged the domains to 100–150 nm, whereas L8-BO reduced them to 30–50 nm, reflecting their opposite effects on phase separation behavior. Similar to the neat NFA films, the GIWAXS patterns of all blended films predominantly exhibited a π–face-on orientation, with pronounced OOP (010) π–π stacking peaks (Figure 6b,c). The CCL values followed the order: YBOV ternary (28.3 Å) > N3 binary (27.1 Å) > L8-BO ternary (26.7 Å) > YBOV binary (26.1 Å) > L8-BO binary (23.1Å), in line with the domain size variations described above [55, 56]. Collectively, the enlarged domains and increased CCL values observed with YBOV incorporation into the N3 binary platform (in contrast to the opposite trend for L8-BO) can be attributed to the generation of additional nucleation sites, confirming that YBOV pre-aggregation acts as nucleation seeds that directly direct film microstructure development. Figure 6d schematically illustrates this heterogeneous nucleation–seeding mechanism of YBOV in the host blend, which facilitates an increased fibril content and enhanced crystallite quality.

To further substantiate the pre-aggregation–driven seeding effect of YBOV, its incorporation into various host platforms (e.g., PM6:N3, PM6:BTP-eC9, and D18:L8-BO) was systematically investigated, and the corresponding photovoltaic properties were evaluated in detail (Figure 6e, Figures S17, S18, S19, and Table S7). The OSCs based on these host platforms were optimized following previously reported protocols to ensure a fair comparison. The obtained PCEs were 16.29% (PM6:N3), and 17.04% (D18:L8-BO), and 16.93% (PM6:BTP-eC9), respectively, which are in close agreement with values reported in the literature. In the above morphology and crystallinity experiments, ternary systems incorporating YBOV in excess of 30 wt.% exhibited a clear reduction in both domain sizes (Figure S21), suggesting that excessive loading disrupts the delicate balance of phase separation and crystallization. This observation highlights that the pre-aggregation–driven seeding effect of YBOV is most effectively manifested at an optimal incorporation level in ternary systems, where pre-aggregation can serve as nucleation centers without over-saturating the host matrix. On this basis, we carried out additional experiments across a range of optimized host platforms, incorporating up to 30 wt.% YBOV. Remarkably, in all host systems examined, the inclusion of YBOV led to improved device performance, with PCEs increasing to 16.71% (PM6:N3), 18.03% (D18:L8-BO), and 19.67% (PM6:BTP-eC9 with 2PACz). These consistent enhancements not only validate the role of YBOV as an effective pre-aggregation–driven seeding agent but also demonstrate its broad versatility and universal applicability in modulating microstructural evolution for OSCs.

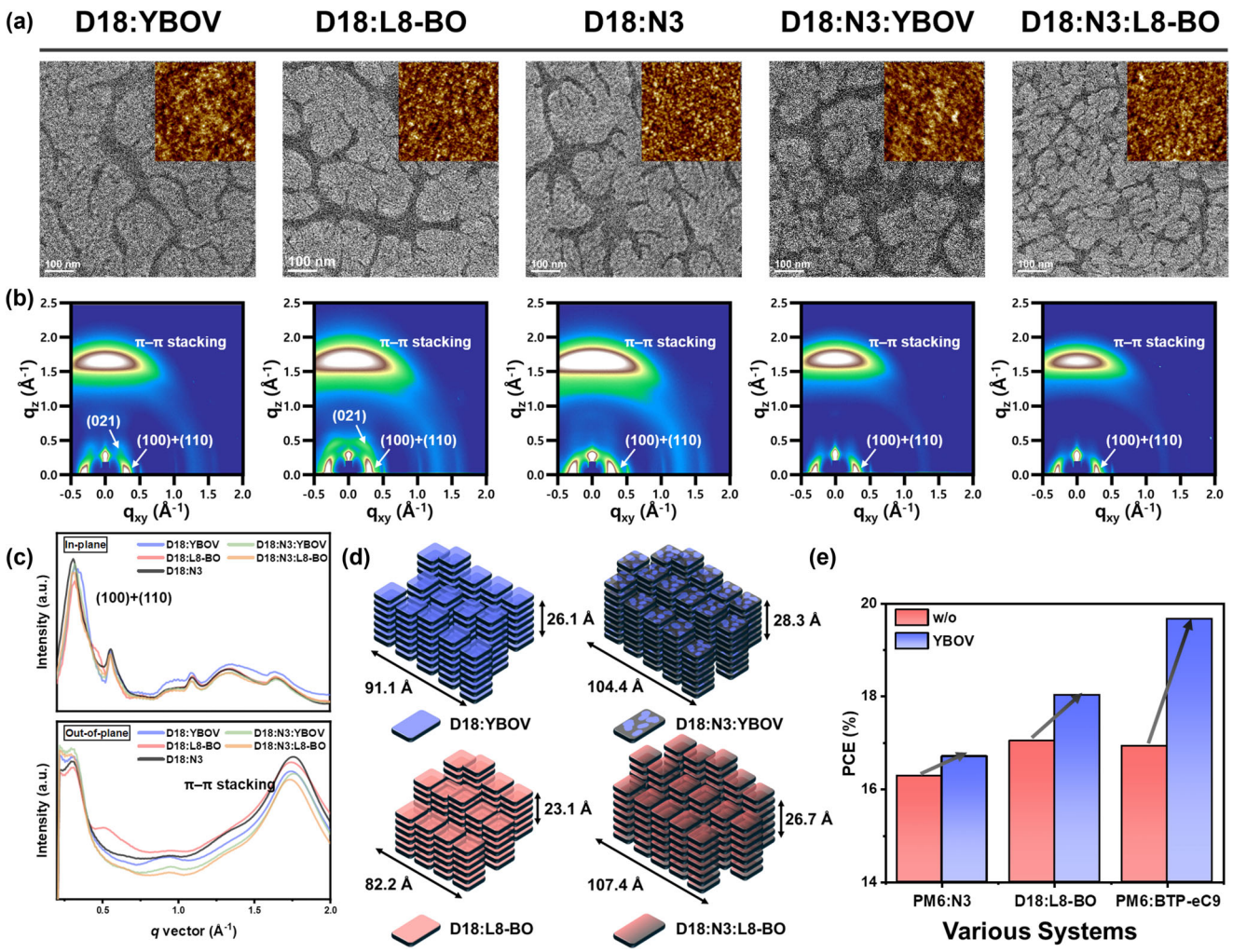

FIGURE 6 | (a) The TEM and AFM images of the blend films. (b) 2D GIWAXS patterns of the blend films. (c) GIWAXS line-cut profiles of the blend films. (d) Schematic illustration of the packing characteristics of the blend films. (e) PCEs obtained from various platforms.

3 | Conclusion

In summary, YBOV, a newly designed NFA incorporating sp^2-hybridized branched inner side chains replacing the conventional sp^3 branches of L8-BO, was synthesized and thoroughly characterized. Unlike L8-BO, YBOV displayed a pronounced propensity for pre-aggregation in solution, as verified by UV–vis, NMR, and HMBC analyses. This pre-aggregation behavior translated into solid films with superior molecular packing and enhanced crystallinity, driven by a thermodynamically favored core–terminal dimer that established continuous terminal pathways and imparted higher crystal density relative to L8-BO. These structural merits directly led to superior photovoltaic performance, with the optimized green-solvent-processed YBOV-based ternary OSC achieving a best PCE of 19.67% through concurrent enhancement of J_{SC} and retention of high V_{OC}. Using *XGBoost*-based ML framework with ECFP descriptors, the predicted J_{SC} , FF, and PCE values showed good agreement with experimental results, albeit with a slight upward bias; in contrast, anomalous V_{OC} behavior arose from pre-aggregation–driven seeding effects that lie beyond the scope of current ML models. In-depth analyses clearly demonstrated that the pre-aggregation–driven seeding effects imparted by YBOV's sp^2-hybridized side chains in given ternary systems promote enlarged domain sizes, enhanced crystallinity, and more efficient charge transport, thereby boosting device performance across diverse host platforms. This work represents the first demonstration of sp^2-hybridized branched side chains, whose pre-aggregation imparts a unique pre-aggregation–driven seeding effect, providing a broadly applicable molecular design strategy for high-performance OSCs.

Acknowledgements

We thank UNIST Office of Research Facilities and Training (ResFacT) for support in using the equipment. This work was supported by the Nano & Material Technology Development Program through the National Research Foundation of Korea (NRF), funded by the Ministry of Science and ICT (RS-2025-25442266) (50% contribution to this work) and the InnoCORE program of the Ministry of Science and ICT (1.260007.01).

Conflicts of Interest

The authors declare no conflict of interest.

Data Availability Statement

CCDC 2482014 contains the supplementary crystallographic data for this paper. These data can be obtained free of charge from The Cambridge Crystallographic Data Centre via www.ccdc.cam.ac.uk/data_request/cif.

References

1. J. Cheng, C. Guo, L. Wang, et al., "Device Engineering of Non-fullerene Organic Photovoltaics with Extrapolated Operational T80 Lifetime over 45,000 h in Air," *Joule* 8 (2024): 2250–2264, https://doi.org/10.1016/j.joule.2024.05.014.

2. Y. Cho, Z. Sun, K. M. Lee, et al., "CF3-Terminated Side Chain Enables Efficiencies Surpassing 18.2% and 16.1% in Small- and Large-Scale Manufacturing of Organic Solar Cells," *ACS Energy Letters* 8 (2023): 96–106, https://doi.org/10.1021/acsenergylett.2c02140.

3. S. Jung, U. J. Yang, J. Oh, et al., "Transfer Printing of Photoactive Layer Enabling Efficient, Wearable, and Dual-Function Organic Solar Cell Modules for a Wireless Healthcare Monitoring System," *Advanced Functional Materials* 34 (2024): 2406200, https://doi.org/10.1002/adfm.202406200.

4. T. L. H. Mai, Z. Sun, S. Kim, et al., "Open-air, Green-solvent Processed Organic Solar Cells with Efficiency Approaching 18% and Exceptional Stability," *Energy & Environmental Science* 17 (2024): 7435–7444, https://doi.org/10.1039/D4EE01944J.

5. S. Yang, X. Huang, Y. Cho, et al., "Efficient Semitransparent Organic Solar Modules with Exceptional Diurnal Stability through Asymmetric Interaction Induced by Symmetric Molecular Structure," *Angewandte Chemie International Edition* 64 (2025): 202424287, https://doi.org/10.1002/anie.202424287.

6. M. Zhang, B. Chang, R. Zhang, et al., "Tethered Small-Molecule Acceptor Refines Hierarchical Morphology in Ternary Polymer Solar Cells: Enhanced Stability and 19% Efficiency," *Advanced Materials* 36 (2024): 2308606, https://doi.org/10.1002/adma.202308606.

7. W. Zhang, C. Sun, I. Angunawela, et al., "16.52% Efficiency All-Polymer Solar Cells with High Tolerance of the Photoactive Layer Thickness," *Advanced Materials* 34 (2022): 2108749, https://doi.org/10.1002/adma.202108749.

8. X. Huang, X. Ren, Y. Cheng, et al., "Collaborative Regulation Strategy of Donor and Acceptor Analogues Realizes Multifunctional Semitransparent Organic Solar Cells with Excellent Comprehensive Performance," *Energy & Environmental Science* 17 (2024): 2825–2836, https://doi.org/10.1039/D3EE04476A.

9. C. Chen, L. Wang, W. Xia, et al., "Molecular Interaction Induced Dual Fibrils towards Organic Solar Cells with Certified Efficiency over 20%," *Nature Communications* 15 (2024): 6865, https://doi.org/10.1038/s41467-024-51359-w.

10. H. Chen, Y. Huang, R. Zhang, et al., "Organic Solar Cells with 20.82% Efficiency and High Tolerance of Active Layer Thickness through Crystallization Sequence Manipulation," *Nature Materials* 24 (2025): 444–453, https://doi.org/10.1038/s41563-024-02062-0.

11. Y. Cho, Z. Sun, G. Li, et al., "CF3-Functionalized Side Chains in Nonfullerene Acceptors Promote Electrostatic Interactions for Highly Efficient Organic Solar Cells," *Journal of the American Chemical Society* 147 (2025): 758–769, https://doi.org/10.1021/jacs.4c13471.

12. J. Yuan, Y. Zhang, L. Zhou, et al., "Single-Junction Organic Solar Cell with over 15% Efficiency Using Fused-Ring Acceptor with Electron-Deficient Core," *Joule* 3 (2019): 1140–1151, https://doi.org/10.1016/j.joule.2019.01.004.

13. J. Deng, J. Liu, C. Jin, et al., "Double-Gene″ Small Molecule as Guest Component Promotes the Efficiency of Organic Solar Cells beyond 19.5 %," *Angewandte Chemie International Edition* 64 (2025): 202420385, https://doi.org/10.1002/anie.202420385.

14. M. Du, N. Sun, H. Cheng, et al., "Multiple-Birth-Acceptor: Easily-Synthesized Mixture for Easily-Fabricated Quaternary Organic Solar Cells with beyond 20% Efficiency," *Angewandte Chemie* 137 (2025): 202515114, https://doi.org/10.1002/ange.202515114.

15. J. Zhu, R. Zeng, E. Zhou, et al., "A Refined Bulk P–I–N Structure in all-Polymer Solar Cells To Achieve 20.1% Efficiency and Improved Stability," *Journal of the American Chemical Society* 147 (2025): 24491–24501, https://doi.org/10.1021/jacs.5c04656.

16. Y. Fu, T. H. Lee, Y.-C. Chin, et al., "Molecular Orientation-dependent Energetic Shifts in Solution-Processed Non-fullerene Acceptors and Their Impact on Organic Photovoltaic Performance," *Nature Communications* 14 (2023): 1870, https://doi.org/10.1038/s41467-023-37234-0.

17. H. Chen, R. Zhang, X. Chen, et al., "A Guest-assisted Molecular-organization Approach for >17% Efficiency Organic Solar Cells Using Environmentally Friendly Solvents," *Nature Energy* 6 (2021): 1045–1053.

18. H. Bin, Y. Yang, Z. Peng, et al., "Effect of Alkylsilyl Side-Chain Structure on Photovoltaic Properties of Conjugated Polymer Donors," *Advanced Energy Materials* 8 (2018): 1702324, https://doi.org/10.1002/aenm.201702324.

19. Y. Chen, Y. Li, W. Zhou, et al., "Y6-Derived Non-fullerene Acceptors with Unsaturated Alkyl Side Chains Enabling Improved Molecular Packing for Highly Efficient Additive-Free Organic Solar Cells," *Chemistry of Materials* 36 (2024): 11606–11617, https://doi.org/10.1021/acs.chemmater.4c02548.

20. Y. Cui, H. Yao, J. Zhang, et al., "Single-Junction Organic Photovoltaic Cells with Approaching 18% Efficiency," *Advanced Materials* 32 (2020): 1908205, https://doi.org/10.1002/adma.201908205.

21. J. Guo, S. Qin, J. Zhang, et al., "Asymmetric Small-molecule Acceptor Enables Suppressed Electron-Vibration Coupling and Minimized Driving Force for Organic Solar Cells," *Nature Communications* 16 (2025): 1503, https://doi.org/10.1038/s41467-025-56799-6.

22. K. Jiang, Q. Wei, J. Y. L. Lai, et al., "Alkyl Chain Tuning of Small Molecule Acceptors for Efficient Organic Solar Cells," *Joule* 3 (2019): 3020–3033, https://doi.org/10.1016/j.joule.2019.09.010.

23. D. Kroh, F. Eller, K. Schötz, et al., "Identifying the Signatures of Intermolecular Interactions in Blends of PM6 with Y6 and N4 Using Absorption Spectroscopy," *Advanced Functional Materials* 32 (2022): 2205711, https://doi.org/10.1002/adfm.202205711.

24. J. Qin, Q. Yang, J. Oh, et al., "Volatile Solid Additive-Assisted Sequential Deposition Enables 18.42% Efficiency in Organic Solar Cells," *Advanced Science* 9 (2022): 2105347, https://doi.org/10.1002/advs.202105347.

25. D. Won, S.-H. Kang, J. Park, et al., "Low-Temperature Processed Efficient and Reproducible Blade-Coating Organic Photovoltaic Devices with γ -Position Branched Inner Side Chains-Containing Nonfullerene Acceptor," *Small Science* 4 (2024): 2400034, https://doi.org/10.1002/smsc.202400034.

26. S. Zahra, S. Lee, M. Jahankhan, et al., "Inner/Outer Side Chain Engineering of Non-Fullerene Acceptors for Efficient Large-Area Organic Solar Modules Based on Non-Halogenated Solution Processing in Air," *Advanced Science* 11 (2024): 2405716, https://doi.org/10.1002/advs.202405716.

27. B. Zhang, M. Jiang, P. Mao, et al., "Manipulating Alkyl Inner Side Chain of Acceptor for Efficient as-Cast Organic Solar Cells," *Advanced Materials* 36 (2024): 2405718, https://doi.org/10.1002/adma.202405718.

28. J. Sun, L. Zhong, Z. Sun, et al., "Functional Role of Dihalogenated Benzothiadiazole Volatile Solid Additives on Crystallization in Photoactive for High-performance Organic Solar Cells," *Materials Today Chemistry* 49 (2025): 103038, https://doi.org/10.1016/j.mtchem.2025.103038.

29. K. Stewart, K. Pagano, E. Tan, et al., "Understanding Effects of Alkyl Side-Chain Density on Polaron Formation via Electrochemical Doping in Thiophene Polymers," *Advanced Materials* 36 (2024): 2211184, https://doi.org/10.1002/adma.202211184.

30. A. J. Schwalb, C. Naranjo, A. Fernández-Alarcón, et al., "Unraveling Pathway Complexity in the Supramolecular Polymerization of Z-Shaped

Perylenediimides: from Kinetic H-Aggregates to Thermodynamic Null Supramolecular Polymers," *Journal of the American Chemical Society* 147 (2025): 25024–25034, https://doi.org/10.1021/jacs.5c08436.

31. X. Han, F. Li, Z. He, et al., "Double Rabi Splitting in Methylene Blue Dye-Ag Nanocavity," *Nanophotonics* 11 (2022): 603–611, https://doi.org/10.1515/nanoph-2021-0697.

32. X. Xu, G. Zhang, L. Yu, R. Li, and Q. Peng, "P3HT-Based Polymer Solar Cells with 8.25% Efficiency Enabled by a Matched Molecular Acceptor and Smart Green-Solvent Processing Technology," *Advanced Materials* 31 (2019): 1906045, https://doi.org/10.1002/adma.201906045.

33. P. Wilhelm, D. Blank, J. M. Lupton, and J. Vogelsang, "Control of Intrachain Morphology in the Formation of Polyfluorene Aggregates on the Single-Molecule Level," *Chemphyschem* 21 (2020): 961–965, https://doi.org/10.1002/cphc.202000118.

34. V. Corne, A. M. Sarotti, C. Ramirez de Arellano, R. A. Spanevello, and A. G. Suárez, "Experimental and Theoretical Insights in the Alkene–arene Intramolecular π-stacking Interaction," *Beilstein Journal of Organic Chemistry* 12 (2016): 1616–1623, https://doi.org/10.3762/bjoc.12.158.

35. X. Lin, M. Suzuki, M. Gushiken, et al., "High-fidelity Self-assembly Pathways for Hydrogen-bonding Molecular Semiconductors," *Scientific Reports* 7 (2017): 43098, https://doi.org/10.1038/srep43098.

36. Z.-P. Yu, Z.-X. Liu, F.-X. Chen, et al., "Simple Non-fused Electron Acceptors for Efficient and Stable Organic Solar Cells," *Nature Communications* 10 (2019): 2152, https://doi.org/10.1038/s41467-019-10098-z.

37. S. Luo, C. Li, J. Zhang, et al., "Auxiliary Sequential Deposition Enables 19%-efficiency Organic Solar Cells Processed from Halogen-free Solvents," *Nature Communications* 14 (2023): 6964, https://doi.org/10.1038/s41467-023-41978-0.

38. C. Wang, X. Ma, Y.-F. Shen, et al., "Unique Assembly of Giant Star-shaped Trimer Enables Non-halogen Solvent-fabricated, Thermal Stable, and Efficient Organic Solar Cells," *Joule* 7 (2023): 2386–2401, https://doi.org/10.1016/j.joule.2023.09.001.

39. C. Li, J. Zhou, J. Song, et al., "Non-fullerene Acceptors with Branched Side Chains and Improved Molecular Packing to Exceed 18% Efficiency in Organic Solar Cells," *Nature Energy* 6 (2021): 605–613, https://doi.org/10.1038/s41560-021-00820-x.

40. D. Li, N. Deng, Y. Fu, et al., "Fibrillization of Non-Fullerene Acceptors Enables 19% Efficiency Pseudo-Bulk Heterojunction Organic Solar Cells," *Advanced Materials* 35 (2023): 2208211, https://doi.org/10.1002/adma.202208211.

41. Z. Sun, H. Ma, T. L. H. Mai, J. Park, S. Jeong, and C. Yang, "Nanoscale Balance of Energy Loss and Quantum Efficiency for High-Efficiency Polythiophene-Based Organic Solar Cells," *ACS Nano* 19 (2025): 1026–1035, https://doi.org/10.1021/acsnano.4c12705.

42. Z. Sun, H. Ma, S. Yang, et al., "Insight into Designing High-Performance Polythiophenes for Reduced Urbach Energy and Nonradiative Recombination in Organic Solar Cells," *Advanced Functional Materials* 34 (2024): 2403093, https://doi.org/10.1002/adfm.202403093.

43. W. Sun, Y. Zheng, K. Yang, et al., "Machine Learning–assisted Molecular Design and Efficiency Prediction for High-performance Organic Photovoltaic Materials," *Science Advances* 5 (2019): aay4275, https://doi.org/10.1126/sciadv.aay4275.

44. Q. Zhang, Y. J. Zheng, W. Sun, et al., "High-Efficiency Non-Fullerene Acceptors Developed by Machine Learning and Quantum Chemistry," *Advanced Science* 9 (2022): 2104742, https://doi.org/10.1002/advs.202104742.

45. D. Rogers and M. Hahn, "Extended-Connectivity Fingerprints," *Journal of Chemical Information and Modeling* 50 (2010): 742–754, https://doi.org/10.1021/ci100050t.

46. G.-H. Kim, C. Lee, K. Kim, and D.-H. Ko, "Novel Structural Feature-descriptor Platform for Machine Learning to Accelerate the Development of Organic Photovoltaics," *Nano Energy* 106 (2023): 108108, https://doi.org/10.1016/j.nanoen.2022.108108.

47. D. Hu, H. Tang, C. Chen, et al., "Insights into Preaggregation Control of Y-Series Nonfullerene Acceptors in Liquid State for Highly Efficient Binary Organic Solar Cells," *Advanced Materials* 36 (2024): 2402833, https://doi.org/10.1002/adma.202402833.

48. Y. Cho, B. Lee, S. Jung, et al., "Role of Simultaneous Thermodynamic and Kinetic Variables in Optimizing Blade-coated Organic Solar Cells," *Energy & Environmental Science* 16 (2023): 6035–6045, https://doi.org/10.1039/D3EE01189E.

49. Y. Kim, S. Kim, S. Lee, et al., "Solid Additive for Manipulating the Lamellar-stacking Phases of Donor and π-stacking Phases of Acceptor and Its Recycling Implementation in Organic Solar Cells," *Chemical Engineering Journal* 503 (2025): 158329, https://doi.org/10.1016/j.cej.2024.158329.

50. J. Park, S. Jeong, Z. Sun, et al., "Triadic Halobenzene Processing Additive Combined Advantages of both Solvent and Solid Types for Efficient and Stable Organic Solar Cells," *Small* 20 (2024): 2405415, https://doi.org/10.1002/smll.202405415.

51. K. Roger, E. Sparr, and H. Wennerström, "Evaporation, Diffusion and Self-assembly at Drying Interfaces," *Physical Chemistry Chemical Physics* 20 (2018): 10430–10438, https://doi.org/10.1039/C8CP00305J.

52. M. H. Gehlen, "The Centenary of the Stern-Volmer Equation of Fluorescence Quenching: from the Single Line Plot to the SV Quenching Map," *Journal of Photochemistry and Photobiology C: Photochemistry Reviews* 42 (2020): 100338, https://doi.org/10.1016/j.jphotochemrev.2019.100338.

53. M. Günther, N. Kazerouni, D. Blätte, et al., "Models and Mechanisms of Ternary Organic Solar Cells," *Nature Reviews Materials* 8 (2023): 456–471.

54. L. Zhu, M. Zhang, J. Xu, et al., "Single-junction Organic Solar Cells with over 19% Efficiency Enabled by a Refined Double-fibril Network Morphology," *Nature Materials* 21 (2022): 656–663, https://doi.org/10.1038/s41563-022-01244-y.

55. S. Jeong, Z. Sun, Y. Cho, et al., "3D Conjugated Nonflat Biphenyl Side Chains: Their Exclusive Role in Inducing Negative Electrostatic Potential in Efficient Organic Solar Cells," *Small* 21 (2025): 09667.

56. Z. Wang, Z. Peng, Z. Xiao, et al., "Thermodynamic Properties and Molecular Packing Explain Performance and Processing Procedures of Three D18:NFA Organic Solar Cells," *Advanced Materials* 32 (2020): 2005386, https://doi.org/10.1002/adma.202005386.

Supporting Information

Additional supporting information can be found online in the Supporting Information section.

Supporting File: aenm70967-sup-0001-SuppMat.docx.